ACS APPLIED MATERIALS & INTERFACES

Research Article

www.acsami.org

Promising Porous Carbon Derived from Celtuce Leaves with Outstanding Supercapacitance and CO_2 Capture Performance

Rutao Wang,[†,‡,§,⊥] Peiyu Wang,[†,#,⊥] Xingbin Yan,*[,†,‡,⊥] Junwei Lang,[†] Chao Peng,[†] and Qunji Xue[‡]

[†]Laboratory of Clean Energy Chemistry and Materials, [‡]State Key Laboratory of Solid Lubrication, Lanzhou Institute of Chemical Physics, Chinese Academy of Science, Lanzhou 730000, P. R. China

[§]Graduate University of Chinese Academy of Sciences, Chinese of Academy of Sciences, Beijing, 100080, China

[#]Institute of Electronic Information Science and Technology, Lanzhou City University, Lanzhou, 730000, China

Supporting Information

ABSTRACT: Business costs and energy/environmental concerns have increased interested in biomass materials for production of activated carbons, especially as electrode materials for supercapacitors or as solid-state adsorbents in CO_2 adsorption area. In this paper, waste celtuce leaves were used to prepare porous carbon by air-drying, pyrolysis at 600 °C in argon, followed by KOH activation. The as-prepared porous carbon have a very high specific surface area of 3404 m^2/g and a large pore volume of 1.88 cm^3/g. As an electroactive material, the porous carbon exhibits good capacitive performance in KOH aqueous electrolyte, with the specific capacitances of 421 and 273 F/g in three and two-electrode systems, respectively. As a solid-state adsorbent, the porous carbon has an excellent CO_2 adsorption capacity at ambient pressures of up to 6.04 and 4.36 mmol/g at 0 and 25 °C, respectively. With simple production process, excellent recyclability and regeneration stability, the porous carbon that was derived from celtuce leaves is among the most promising materials for high-performance supercapacitors and CO_2 capture.

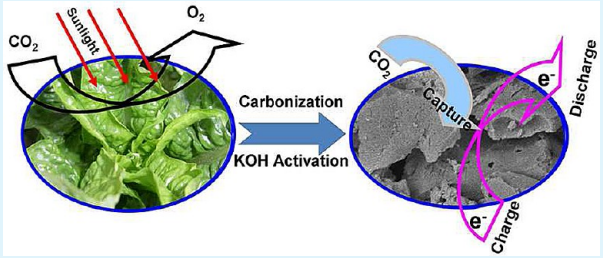

KEYWORDS: *porous carbon, celtuce leaves, supercapacitor, CO_2 capture, biomass, KOH activation*

1. INTRODUCTION

Porous carbon is a promising material for catalyst supports,[1] supercapacitors,[2] adsorbents,[3] among others. This material has attracted much interest because of its numerous exceptional characteristics, including moderate costs, high thermal and chemical stability, hydrophobic surface properties, and high electrical conductivity. To date, several porous carbon materials with different structures and morphologies have been designed and prepared, such as powders, fibers, aerogels, tubes, and monoliths.[4,5] Well-established chemical and/or physical activation methods, including soft and hard template methods,[6−8] chemical vapor deposition,[9] and chemical (KOH, CO_2, NH_3, and H_2O)-activation,[10−13] allow the production of porous carbon with high surface areas (above 1000 m^2/g). Carbon-based supercapacitors exploit the electrostatic separation between electrolyte ions and high-surface area electrodes, typically carbon. This results in energy stored in supercapacitor is linearly proportional to capacitance of its electrodes, making carbon materials with high-surface area crucial.[2] In addition, porous carbon having high surface area can be more practical where physisorption of CO_2 is favored over chemisorption, which in turn greatly reduces the energy needed for regeneration. The use of biomass materials to produce porous carbon becomes of interest when business costs, wide availability, and energy/environmental concern are considered.[11] These porous carbons are generally produced by the carbonization of the original biomass materials and the further chemical or physical activation. To date, various biomass-derived porous carbons, such as from fungi,[14] corn grain,[15] lignocellulosic materials,[16,17] fish scales,[18] and starch,[19] have been reported. These materials have showed great potential as electrode materials for supercapacitors or as solid-state adsorbents in CO_2 capture.

The herbaceous plant celtuce (*Lactuca sativa* L. var. *asparagina, augustana, or angustata*) has been widely used as food because of its worldwide abundance. Its outer leaves may be eaten in salads at the younger plant stages, whereas the translucent green central core may be eaten fresh or in salads at any stage of the plant. In China, most people eat the fleshy stem by boiling or stewing, whereas the leaves are usually discarded because of their slightly bitter taste (Figure S1 in the Supporting Information). Thus, the potential applications of celtuce leaves in energy storage and CO_2 capture may have been overlooked.

In this paper, we used waste celtuce leaves to prepare porous carbon by air-drying, pyrolysis at 600 °C in argon, and KOH activation. By optimizing the carbonization temperature to balance the porosity and capacitance, the resulting porous

Received: July 10, 2012
Accepted: October 25, 2012
Published: October 25, 2012

carbon shows an extremely high specific surface area of up to 3400 m^2/g as well as excellent capacitive performance with a specific capacitance of 421 and 273 F/g in three and two-electrode systems, respectively. As a solid-state adsorbent, it has a high CO_2 adsorption capacity at ambient pressures of 6.04 and 4.36 mmol/g at temperatures of 0 and 25 °C, respectively. Given these excellent capacitive properties, CO_2 capture capacity, ease of preparation, abundant resources, excellent recyclability, and regeneration stability, the porous carbon derived from celtuce leaves has a potential for supercapacitive electrode materials and CO_2 adsorbents.

2. EXPERIMENTAL SECTION

Preparation of the Celtuce Leaf-Derived Porous Carbon. The waste celtuce leaves that were collected from a local vegetable market were air-dried, cut into pieces, and pyrolyzed at 600 °C under an argon atmosphere to obtain the pyrolytic celtuce leaves (denoted as CL). The KOH activation step was performed as follows: typically, 0.4 g of ground CL was impregnated with 1.6 g of KOH in an aqueous solution by sonication, which was followed by evaporation step at 80 °C. The dried CL/KOH mixture was then heated at 800 °C for 1 h under an argon atmosphere. After cooling down to room temperature, the sample was washed with 1 M HCl solution and ultrapure water until its pH reached a value of 7. The sample was then dried at 60 °C in air. The final product was denoted as activated celtuce leaves (a-CL). To produce the celtuce leaf-derived porous carbon with the highest capacitance, the carbonization temperature was optimized. Accordingly, a carbonization temperature of 600 °C was determined to be optimal. More details on the optimization are shown in the Supporting Information.

Structural Characterization. Field-emission scanning electron microscopy (FESEM; JSM 6701F) was employed to investigate the surface and cross-sectional morphologies of the as-prepared carbon before and after KOH activation. To investigate the structure and composition of the samples, powder X-ray diffraction (XRD; Rigaku D/Max-2400) was performed using Cu $K\alpha$ radiation. Transmission electron microscopy (TEM; F-30) operated at 300 kV and was used to observe the as-prepared carbon structure and morphology. The surface chemical species of the as-prepared carbon was examined by X-ray photoelectron spectroscope (XPS) using a Perkin-Elmer PHI-5702 multifunctional photoelectron spectrometer (Physical Electronics, USA) with 1486.6 eV radiation as the excitation source. All the XPS spectra were calibrated by using Au $4f_{7/2}$ at 84.0 eV. The nitrogen adsorption−desorption isotherm measurements were performed on a Micromeritics ASAP 2020 M volumetric adsorption analyzer at 77 K. The Brunauer−Emmett−Teller (BET) method was utilized to calculate the specific surface area. The pore-size distribution was determined by a nonlocal density functional method using the nitrogen adsorption data, and assuming a slit pore model. The total pore volume was estimated from the amount adsorbed at a relative pressure of $P/P_0 = 0.99$.

Electrode Preparation and Electrochemical Measurements. The working electrodes were prepared as follows: 80 wt % sample was mixed with 7.5 wt % acetylene black and 7.5 wt % conducting graphite in an agate mortar until a homogeneous black powder was obtained. To this mixture was added 5 wt % poly(tetrafluoroethylene) with a few drops of ethanol. After the solvent was briefly allowed to evaporate, the resulting paste was pressed at 10 MPa to the nickel gauze with a nickel wire for an electric connection. The assembled electrodes were dried for 10 h at 60 °C in air. Each electrode contained about 8 mg of electroactive material and had a geometric surface area of about 1 cm^2.

Electrochemical measurements were performed using an electrochemical working station (CHI660D, Shanghai, China) in a three-electrode system in 2 M KOH aqueous electrolyte at room temperature. A platinum gauze electrode and a saturated calomel electrode served as the counter electrode and the reference electrode, respectively. The average specific capacitance values were calculated from the galvanostatic discharge curves, using the following equation

$$C = I/[(dE/dt)m] \approx I/[(\Delta E/\Delta t)m]\ (\mathrm{F/g})$$

where I is constant discharge current, Δt is the time period for a full discharge, m indicates the mass of the corresponding active electrode material, and ΔE represents the voltage change after a full discharge.

A two-electrode cell configuration was used to measure the performance of supercapacitors with the KOH activated CL materials. A pair of typical electrodes had a weight 4 mg of active materials after drying overnight at ∼60 °C. The two identical electrodes were pressed together and separated by a porous nonwoven cloth separator. An aqueous solution of 2 M KOH was used as the electrolyte. Gravimetric capacitance from galvanostatic charge/discharge was calculated by using the formula

$$C = 4I/(dE/dt) \approx 4I/[(\Delta E/\Delta t) \times m](\mathrm{F/g})$$

CO_2 Capture Measurements. The CO_2 adsorption isotherms of the samples were measured using a Micromeritics ASAP 2020 static volumetric analyzer at 0 and 25 °C. The N_2 adsorption isotherms of the a-CL were measured using a Micromeritics ASAP 2020 static volumetric analyzer at 0 °C. Prior to each adsorption experiment, the sample was degassed for 4 h at 150 °C to ensure that the residual pressure was below 1×10^{-3} mbar. After the samples were cooled down to to 0 or 25 °C, CO_2 was introduced into the system. The CO_2 adsorption capacity in terms of the adsorbed volume under standard temperature and pressure was then recorded. The recycling adsorption test of CO_2 was performed with a simple regeneration by evacuating at 150 °C for 4 h under a pressure of 1×10^{-3} mbar.

3. RESULTS AND DISCUSSION

3.1. SEM and HTEM Analyses. KOH activation has been widely used on graphene,[10] carbon nanotubes,[20] carbide-derived carbon,[21] and mesoporous carbon[22] to increase the surface area and improve the electrochemical performance. When the activation temperature is higher than 400 °C, The chemical reactions are involved into the process: $6\ KOH + 2\ C \rightarrow 2\ K + 3\ H_2 + 2\ K_2CO_3$, and subsequent decomposition of K_2CO_3 and/or reactions of $K/K_2CO_3/CO_2$ with the carbon.[20,23] Given the loss of carbon, a large amount of nanoscale pores are generated in the final products. Figure S2 in the Supporting Information shows the preparation schematic of porous activated carbon derived from the fresh celtuce leaves by air-drying, pyrolysis under an argon atmosphere and KOH activation. The SEM images of the celtuce leaves that were pyrolyzed at 600 °C (Figure 1), specifically the cross-view images, display a continuous, loose but distorted layered microstructure. Such a characteristic structure can facilitate the following KOH impregnation and activation. By comparing the SEM images of the CL sample before and after activation (Figures 1 and 2a, b), it is clear seen that nanoscale pores and local curvature have been generated on/in as-prepared carbon. Figure S3 in the Supporting Information and images c and d in Figure 2 show the typical TEM images of the CL sample before and after KOH activation with different magnifications, respectively. These results further verify that KOH can etch CL and generate a substantial amount of micro/mesopores that are homogeneously distributed throughout the highly porous structure.

3.2. XRD, XPS, and BET Analyses. The XRD patterns of the CL and a-CL samples as shown in Figure 3a, while Figure 3b shows their XPS full-spectra. Several diffraction peaks existing in the XRD pattern of CL, indicating the formation of crystalline inorganic compounds, which come from the trace elements of celtuce leaves. These inorganic compounds might contain potassium, chlorine, fluorine, carbon, and oxygen (Figure 3b). The XRD pattern of a-CL just shows two broad

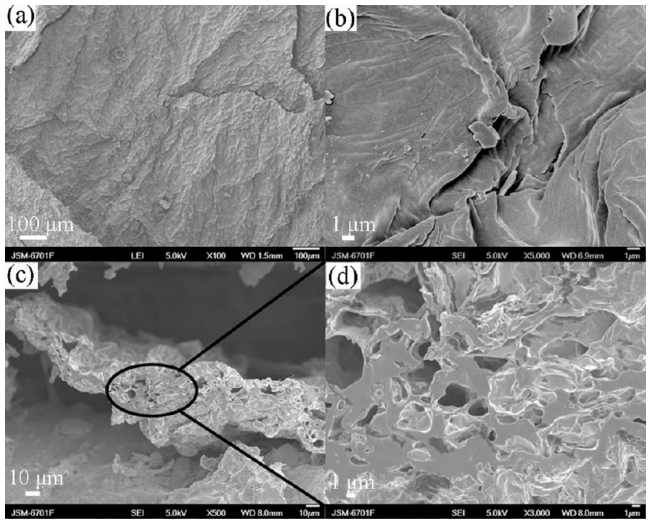

Figure 1. SEM images of carbonated celtuce leaves (CL): (a, b) surface morphology of CL; (c, d) the cross-section morphology of CL.

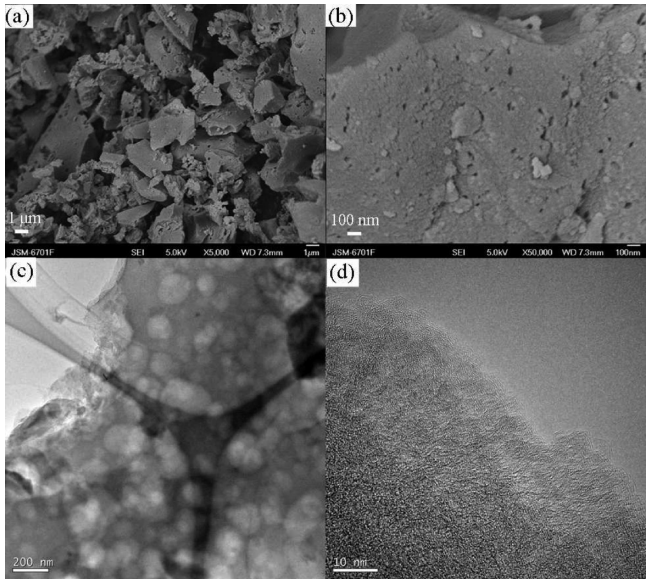

Figure 2. (a, b) SEM images of a-CL; (c, d) TEM images of a-CL with different magnifications.

diffraction peaks at 22 and 43°, which correspond to the (002) and (100) diffraction patterns of amorphous graphitic carbon.

To investigate the causes of the improved pyrolysis temperatures of celtuce leaves, thermal analysis and XPS were performed on the dried and milled leaves. Figure S3 in the Supporting Information shows the different stages on the thermogravimetric analysis (TGA) curves that were obtained with celtuce leaves. The first step (up to 200 °C) is related to desorption of adsorbed water. The next step (200 to 450 °C) is correlated with the decomposition of carbohydrates and cellulose. The last step, which starts at around 450 °C, is essentially related to the elimination of the heteroatoms (such as oxygen) from the carbonaceous matter. After pyrolysis at 600 °C, CL is composed of carbon and hetero atoms (primarily O, Cl, and F) that are uniformly distributed on the surface or within the structure of CL, as detected by XPS (Figure 3b). After KOH activation, its XPS full-spectrum shows two obvious peaks that can be attributed to the dominated carbon and some oxygen. Only ~3.75 wt % O and ~0.56 wt % N are detected in the a-CL sample. Therefore, a mass of uniformly distributed hetero atoms and all inorganic impurities have been removed by KOH activation and the subsequent washing process. The atom removing process follows opening of closed and bottleneck pores, thereby resulting in the CL efficiently transforms into microporous and mesoporous carbon with unusually high specific surface area and interconnected pores with high pore volume.[19] Figure 3c shows the type-IV isotherm that is characteristic for mesoporous materials. The wide capillary condensation step toward higher relative pressure indicates the wide distribution of pore sizes, which is consistence with the TEM results. The KOH activation yields a continuous network of micro/mesopores of extremely small size, ranging from 0.5 to 5 nm, and of large mesopores and/or the textural macropores, ranging from 30 to 60 nm. The pores which are smaller than 5 nm account for over ~90% of the total volume of the a-CL sample as shown in Figure 3d. The a-CL sample shows much higher specific surface area (up to 3400 m^2/g) and larger pore volume (up to 1.88 cm^3/g) than that of CL (only 4.37 m^2/g and 0.06 cm^3/g, respectively).

3.3. Electrochemical Performance. The KOH activation changes the chemical character and the porous structure of CL, including the real surface and its micro/mesopore content, which might have influenced on its electrochemical capacitive performance and CO_2 adsorption capacity. The typical capacitive behavior of a-CL sample, which is present in the form of a rectangular shape of the voltammetry characteristics, is presented in Figure 4a. The rectangular shapes of the CV curves and the slight distortion at the high CV scan rates indicate that the capacitive response comes from the combination of the electric double layer capacitor (EDLC) and redox reactions, which are related to the surface oxygen functionalities of the materials. Figure 4b shows the galvanostatic charge/discharge curves at different current densities. The specific capacitances are calculated from the discharge curves with values of 421, 361, 324, and 293 F/g at the current densities of 0.5, 1, 2, and 5 A/g, respectively. Even at a relatively high current density of 10 A/g, the specific capacitance is still maintained at 262 F/g, thereby exhibiting the good rate capability (as shown in Figure 4c). Moreover, the cycle life of the electrode was monitored by chronopotentiometry measurements at the current density of 5 A/g, as shown in Figure 4d. The specific capacitance decreased slowly at initial stage and then tends to be stable at 93.1% of the initial capacitance after 1600 cycles. Only 6.9% of the initial capacitance is lost after 2000 cycles, indicating that the a-CL has a long cycle life as supercapacitor electrode material.

Using common methods for determining an electrode material's performance for supercapacitors, we also constructed and measured the performance of two-electrode symmetrical supercapacitor cells based on a-CL and a KOH aqueous electrolyte, as shown in Figure 5. The CV curves of a-CL present typical EDLC behavior with the rectangular shape characteristic from 0 to 1 V over a wide range of voltage scan rates. The charge−discharge curves shown in Figure 5b are almost linear and show a typical triangular symmetrical distribution, displaying high capacitive properties. The specific capacitance is ~273 F/g at current densities of 0.5 A/g. At a relatively high current density of 10 A/g, the specific capacitance ~156 F/g is still retained. The Nyquist plot ranging from 100 to 0.01 Hz features a vertical curve and a low faradic charge transfer resistance, indicating a nearly ideal

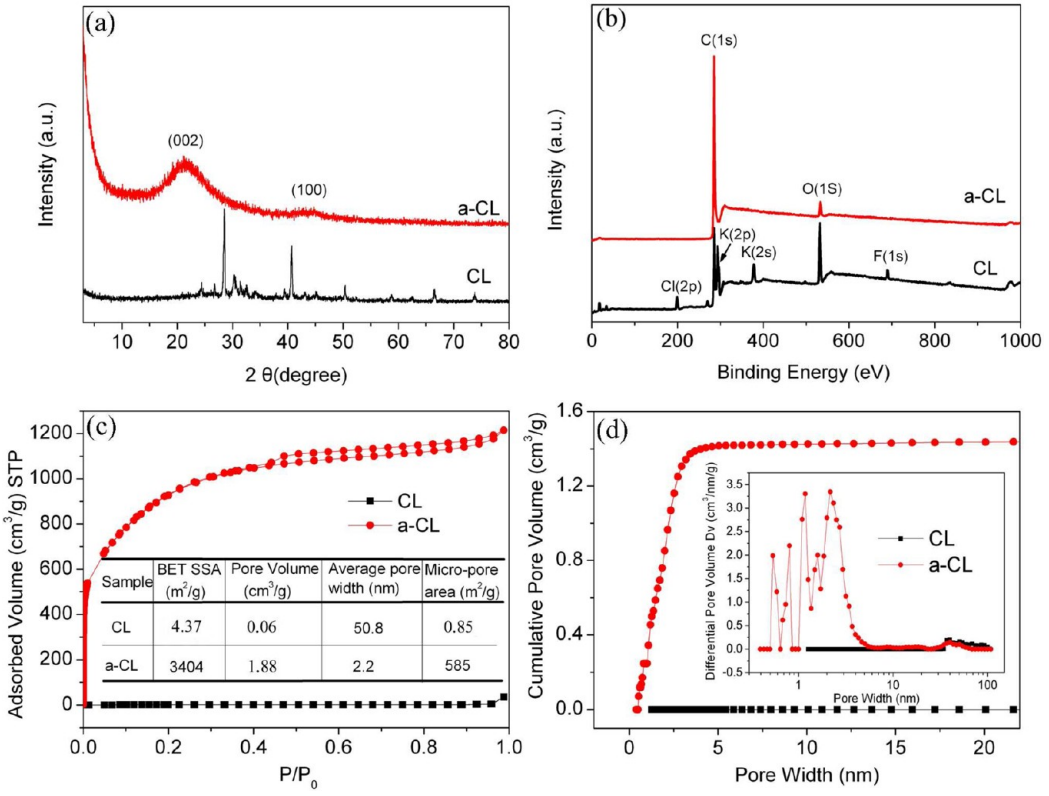

Sample	BET SSA (m^2/g)	Pore Volume (cm^3/g)	Average pore width (nm)	Micro-pore area (m^2/g)
CL	4.37	0.06	50.8	0.85
a-CL	3404	1.88	2.2	585

Figure 3. (a) XRD patterns of CL and a-CL, (b) XPS full-spectra of CL and a-CL; (c, d) the N_2 sorption isotherms and porosity characteristics of a-CL and CL.

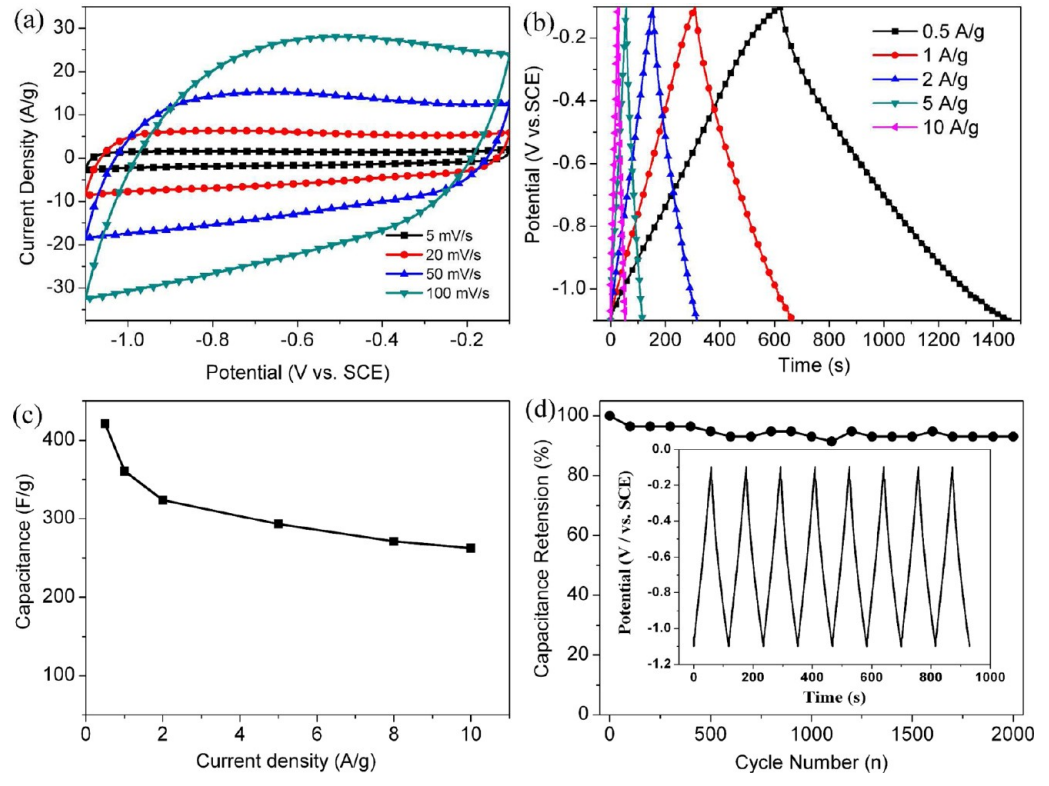

Figure 4. Electrochemical characteristics of a-CL in 2 M KOH aqueous electrolyte in a three-electrode system: (a) CV curves at different scan rates; (b) galvanostatic charge/discharge curves at different current densities; (c) the specific capacitance as a function of discharge current density; (d) capacitance retention at the current density of 5 A/g.

dx.doi.org/10.1021/am302077c | ACS Appl. Mater. Interfaces 2012, 4, 5800−5806

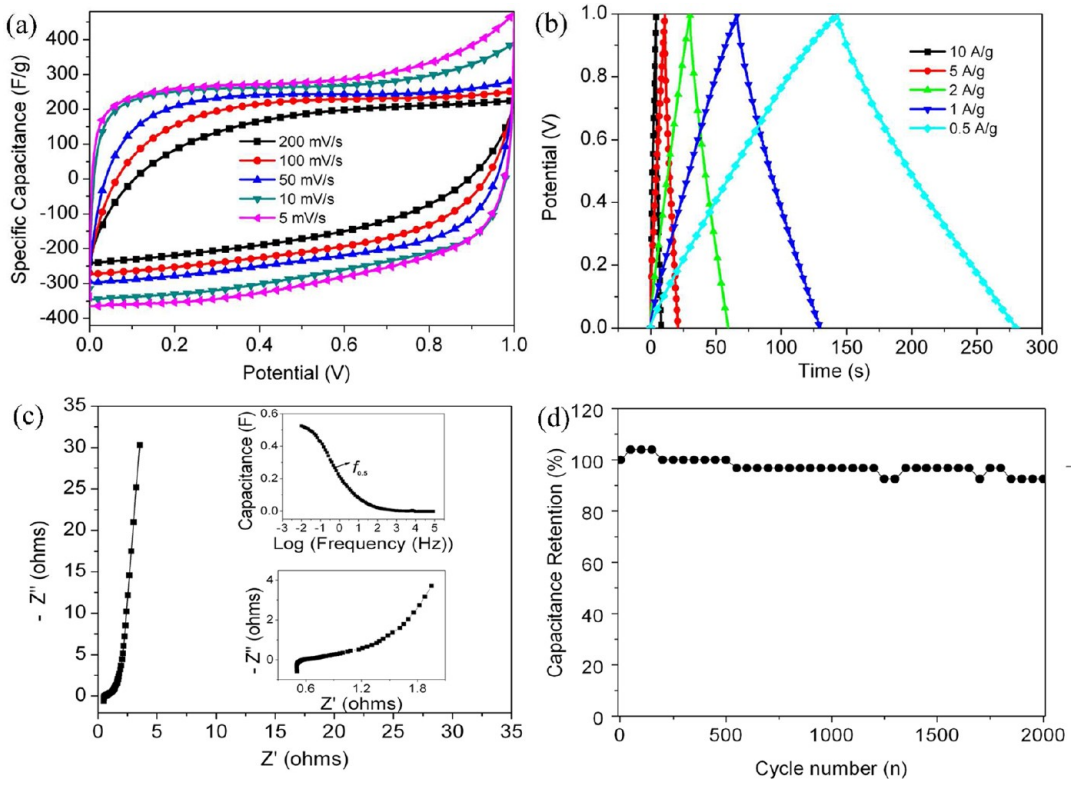

Figure 5. Electrochemical characteristics of a-CL supercapacitor cell: (a) CV curves at different scan rates; (b) galvanostatic charge/discharge curves at different current densities; (c) Nyquist plot, showing the imaginary part versus the real part of impedance. Inset images show the data of high frequency range and frequency response of the gravimetric capacitance of the a-CL supercapacitor; (d) capacitance retention at charge/discharge current density 2 A/g.

capacitive behavior as that of the a-CL electrode material. The internal cell resistance (real Z′ axis from Nyquist plots) was 0.57 Ω (6.84 kHz) in the KOH electrolytes. The capacitance from the electrochemical impedance spectroscopy data as a function of frequency is shown in Figure 5c. The capacitance drops to 50% of its maximum value ($f_{0.5}$), that is, 0.56 Hz, which demonstrates the fast frequency response of the porous carbon in aqueous solution. This porous carbon material is likewise stable (Figure 5d). After 2000 constant charge/discharge cycles at a current density of 2 A/g in KOH aqueous electrolyte, ∼92.6% of its capacitance is retained.

3.4. CO_2 Capture Performance. The CO_2 adsorption isotherms of the a-CL and CL at 0 °C are shown in Figure 6a. The a-CL sample exhibited a relatively high CO_2 adsorption capacity of 6.04 mmol/g at 0 °C under the ambient pressure. The XPS analysis showed that the alkaline element or group is negligible in a-CL. The high specific surface area and the porous structure of a-CL are important in determining the CO_2 adsorption capacity, which has also been evidenced by other reports.[24−29] For comparison, sample CL displays a low CO_2 adsorption capacity of 1.72 mmol/g, which is considerably significant relative to the low specific surface area of CL. The CO_2 storage capacity was similarly determined at ambient temperature (25 °C) as shown in Figure 6a. The a-CL sample exhibited a high CO_2 adsorption capacity at ambient pressure of up to 4.36 mmol/g at 25 °C. This CO_2 adsorption value of a-CL is higher than that of other biomass-derived carbon materials.[30−33] Furthermore, this CO_2 adsorption value of a-CL is still comparable to the most of porous carbon materials that have been doped with nitrogen or functionalized with amine.[24−26,34−36] More details on the comparison of the specific capacitance and the CO_2 adsorption capacity of our porous carbon with other biomass-derived carbons or other typical carbons are included in the Supporting Information.

Under the same experimental conditions, the adsorption capacity of a-CL for N_2 was likewise measured. As shown in Figure 6a, the adsorption capacities of N_2 are much lower as compared with those for CO_2 under the same pressure, reaching a maximum of 0.64 mmol/g under ambient pressure at 0 °C. Thus, at identical pressure for both CO_2 and N_2, the amount of nitrogen adsorbed is only one tenth of the amount of carbon oxide. Therefore, a-CL, even with only minor nitrogen elements, could still be a potential selective adsorbent for CO_2 and N_2 separation, which is consistent with Hao.[24]

Figure 6b shows the CO_2 adsorption isotherms of a-CL at 0 °C for six cycling runs with regeneration. The first three cycling runs (first, second, and third run) were continuously measured, but the subsequent three cycling runs (fourth, fifth, and sixth run) were measured two months later. The CO_2 adsorption capacities are almost maintained under the same conditions for the first three cycling runs, showing that a-CL is highly stable and can be recycled to capture CO_2. The little loss of the capacities for a-CL in the recycling process may be as the result of the low regeneration temperature, which leads to less CO_2 bind tight-binding to the surface of a-CL. The CO_2 adsorption capacities are similarly maintained under the identical conditions for the second three cycling runs, suggesting that the CO_2 adsorption capacities of a-CL are also retained for a long time period.

The high specific capacitance and superior CO_2 adsorption capacity could be attributed to the excellent porous structure of a-CL, with its ultrahigh specific surface area, large pore volume

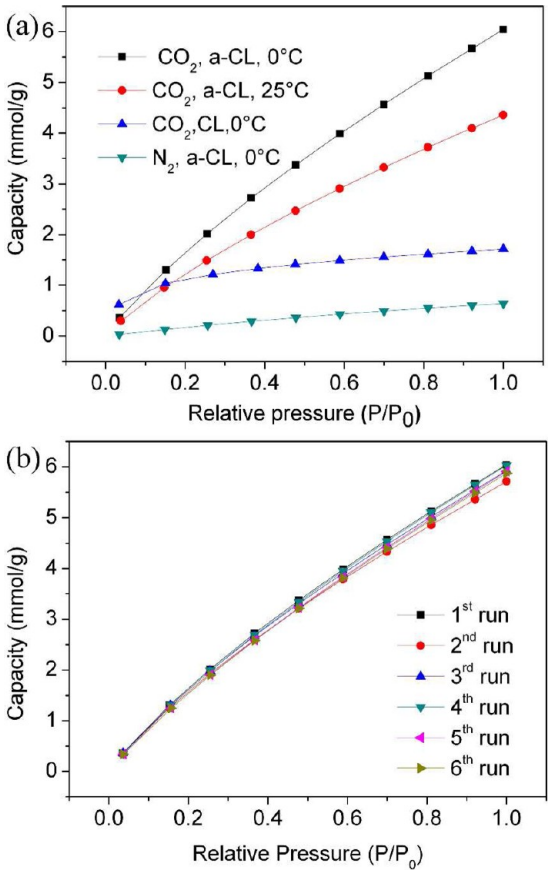

Figure 6. (a) CO_2 uptake isotherms of a-CL at 0 and 25 °C, the CO_2 adsorption isotherm of CL at 0 °C and the N_2 adsorption isotherm of a-CL at 0 °C. (b) CO_2 multicircle adsorption isotherms for a-CL at 0 °C.

and wide pore-size distribution. In a supercapacitor electrode, these advantages can enhance the electrolyte/carbon contact area and facilitate electrolyte penetration and ion diffusion during the electrochemical charging/discharging process.[37,38] Moreover, a certain amount of micropores determines the excellent characteristics of a-CL according to Huang's universal model (electric wire-in cylinder capacitors).[39] As a CO_2 adsorbent, the excellent pore structure of a-CL might favor its superior CO_2 capture performance by facilitating the diffusion of CO_2 into the channels.

4. CONCLUSIONS

Porous carbon with ultrahigh specific surface area, large pore volume, and wide pore-size distribution has been successfully produced from waste celtuce leaves through air-drying, high-temperature pyrolysis, and KOH activation. The as-prepared carbon has the desired electrochemical capacitive properties in KOH aqueous electrolytes and exhibits excellent CO_2 adsorption capacity at ambient pressure. Considering their worldwide abundance and their recyclability, celtuce leaves could be act as a new biomass source of porous carbon materials for high-performance supercapacitors and CO_2 capture.

■ ASSOCIATED CONTENT

Ⓢ Supporting Information

Photographs of waste celtuce leaves, schematic of the preparation of porous carbon, thermogravimetric analysis (TGA) curves of celtuce leaves, microstructure of carbonated celtuce leaves, optimization of carbonization temperature, comparison of specific capacitance and CO_2 adsorption capacity of our porous carbon with other biomass-derived carbons or other typical carbons. This information is available free of charge via the Internet at http://pubs.acs.org/.

■ AUTHOR INFORMATION

Corresponding Author

*Fax: +86-931-4968055. E-mail: xbyan@licp.cas.cn.

Author Contributions

⊥These authors contributed equally to this report. The manuscript was written through contributions of all authors. All authors have given approval to the final version of the manuscript.

Notes

The authors declare no competing financial interest.

■ ACKNOWLEDGMENTS

This work was supported by the Top Hundred Talents Program of Chinese Academy of Sciences and the Youth Science Foundations of Gansu Province (1107RJYA274).

■ REFERENCES

(1) Hiyoshi, N.; Sato, O.; Yamaguchi, A.; Rode, C. V.; Shirai, M. *Green Chem.* **2012**, *14*, 633−638.
(2) Zhai, Y. P.; Dou, Y. Q.; Zhao, D. Y.; Fulvio, P. F.; Mayes, R. T.; Dai, S. *Adv. Mater.* **2011**, *23*, 4828−4850.
(3) Mohan, D.; Pittman, C. U., Jr. *J. Hazard. Mater.* **2007**, *142*, 1−3.
(4) Pandolfo, A. G.; Hollenkamp, A. F. *J. Power Sources.* **2006**, *157*, 11−27.
(5) Liu, C.; Li, F.; Ma, L. P.; Cheng, H. M. *Adv. Mater.* **2010**, *22*, E28−62.
(6) Liang, C. D.; Li, Z. J.; Dai, S. *Angew. Chem., Int. Ed.* **2008**, *47*, 3696−3717.
(7) Kyotani, T.; Ma, Z. X.; Tomita, A. *Carbon* **2003**, *41*, 1451−1459.
(8) Ryoo, R.; Joo, S. H.; Jun, S. *J. Phys. Chem. B* **1999**, *103*, 7743−7746.
(9) Miller, J. R.; Outlaw, R. A.; Holloway, B. C. *Science* **2010**, *329*, 1637−1639.
(10) Zhu, Y. W.; Murali, S.; Stoller, M. D.; Ganesh, K. J.; Cai, W. W.; Ferreira, P. J.; Pirkle, A.; Wallace, R. M.; Cychosz, K. A.; Thommes, M.; Su, D.; Stach, E. A.; Ruoff, R. S. *Science* **2011**, *332*, 1537−1541.
(11) Nandi, M.; Okada, K.; Dutta, A.; Bhaumik, A.; Maruyama, J.; Derks, D.; Uyama, H. *Chem. Commun.* **2012**, *48*, 10283−10285.
(12) Jurcakova, D. H.; Kodama, M.; Shiraishi, S.; Hatori, H.; Zhu, Z. H.; Lu, G. Q. *Adv. Funct. Mater.* **2009**, *19*, 1800−1809.
(13) Górka, J.; Jaroniec, M. *Carbon* **2011**, *49*, 154−160.
(14) Zhu, H.; Wang, X. L.; Yang, F.; Yang, X. R. *Adv. Mater.* **2011**, *23*, 2745−2748.
(15) Balathanigaimani, M. S.; Shim, W. G.; Lee, M. J.; Kim, C.; Lee, J. W.; Moon, H. *Electrochem. Commun.* **2008**, *10*, 868−871.
(16) Wu, F. C.; Tseng, R. L.; Hu, C. C.; Wang, C. C. *J. Power Sources.* **2004**, *138*, 351−359.
(17) Plaza, M. G.; García, S.; Rubiera, F.; Pis, J. J.; Pevida, C. *Sep. Purif. Technol.* **2011**, *80*, 96−104.
(18) Chen, W. X.; Zhang, H.; Huang, Y. Q.; Wang, W. K. *J. Mater. Chem.* **2010**, *20*, 4773−4775.
(19) Wei, L.; Sevilla, M.; Fuertesm, A. B.; Mokaya, R.; Yushin, G. *Adv. Energy Mater.* **2011**, *1*, 356−361.
(20) Raymundo-Piñero, E.; Azaïsa, P.; Cacciaguerraa, T.; Cazorla-Amorósb, D.; Linares-Solanob, A.; Béguin, F. *Carbon* **2005**, *43*, 786−795.
(21) Portet, C.; Lillo-Ródenas, M. Á.; Linares-Solano, A.; Gogotsi, Y. *Phys. Chem. Chem. Phys.* **2009**, *11*, 4943−4945.

(22) Jin, J.; Tanaka, S.; Egashira, Y.; Nishiyama, N. *Carbon* **2010**, *48*, 1985−1989.
(23) Lillo-Ródenas, M. A.; Cazorla-Amorós, D.; Linares-Solano, A. *Carbon* **2003**, *41*, 267−275.
(24) Hao, G. P.; Li, W. C.; Qian, D.; Lu, A. H. *Adv. Mater.* **2010**, *22*, 853−857.
(25) Shen, W. Z.; Zhang, S. C.; He, Y.; Li, J.; Fan, W. B. *J. Mater. Chem.* **2011**, *21*, 14036−14040.
(26) Xia, Y.; Mokaya, R.; Walker, G. S.; Zhu, Y. *Adv. Energy Mater.* **2011**, *1*, 678−683.
(27) Hu, X.; Radosz, M.; Cychosz, K. A.; Thommes, M. *Environ. Sci. Technol.* **2011**, *45*, 7068−7074.
(28) Hao, G. P.; Li, W. C.; Lu, A. H. *J. Mater. Chem.* **2011**, *21*, 6447−6451.
(29) Hwang, C. C.; Jin, Z.; Lu, W.; Sun, Z. Z.; Alemany, L. B.; Lomeda, J. R.; Tour, J. M. *ACS Appl. Mater. Interfaces* **2011**, *3*, 4782−4786.
(30) Plaza, M. G.; García, S.; Rubiera, F.; Pis, J. J.; Pevida, C. *Sep. Purif. Technol.* **2011**, *80*, 96−104.
(31) Boonpoke, A.; Chiarakorn, S.; Laosiripojana, N.; Towprayoon, S.; Chidthaisong, A. *J. Sust. Energ. Environ.* **2011**, *2*, 77−81.
(32) Shafeeyan, M. S.; Daud, W. M. A. W.; Houshmand, A.; Arami-Niya, A. *Appl. Surf. Sci.* **2011**, *257*, 3936−3942.
(33) Xing, W.; Liu, C.; Zhou, Z.; Zhang, L.; Zhou, J.; Zhuo, S.; Yan, Z. F.; Gao, H.; Wang, G. Q.; Qiao, Z. Q. *Energy Environ. Sci.* **2012**, *5*, 7323−7327.
(34) Zhang, Z.; Xu, M.; Wang, H.; Li, Z. *Chem. Eng. J.* **2010**, *160*, 571−577.
(35) Pevida, C.; Drage, T. C.; Snape, C. E. *Carbon* **2008**, *46*, 1464−1474.
(36) Wang, L.; Yang, R. T. *J. Phys. Chem. C* **2012**, *116*, 1099−1106.
(37) Simon, P.; Gogotsi, Y. *Philos. Trans. R. Soc. London* **2010**, *368*, 3457−3467.
(38) Chmiola, J.; Yushin, G.; Gogotsi, Y.; Portet, C.; Simon, P.; Taberna, P. L. *Science* **2006**, *313*, 1760−1763.
(39) Huang, J. S.; Sumpter, B. G.; Meunier, V. *Chem.—Eur. J.* **2008**, *14*, 6614−6626.